Fuel Cell-Supercapacitor Topologies Benchmark for a Three-Wheel Electric Vehicle Powertrain

A. Macias[1,2,4]*, M. Kandidayeni[2,3,4], L. Boulon[1,2], J. Trovão[3,4]

[1]Université du Québec à Trois-Rivières, Trois-Rivières, QC, Canada

[2]Institut de Recherche sur l'Hydrogène, UQTR, Trois-Rivières, QC, Canada

[3]Université de Sherbrooke, Sherbrooke, QC, Canada

[4]e-TESC Laboratory, University of Sherbrooke, Sherbrooke, QC, Canada

Abstract

This paper compares three optimal hybrid energy system configurations, namely full-active, semi-active and passive, for the particular purpose of assessing the viability of utilizing the passive architecture in a three-wheel electric vehicle, composed of a fuel cell (FC) and a supercapacitor. In this respect, the characteristics of these configurations are investigated through three steps. Firstly, the mathematical model of each component is developed by employing experimental data. Subsequently, the optimal size of each topology is determined by a two-step optimization approach. This approach is based on the optimized sizing of power sources, employing a metaheuristic optimization algorithm, and optimal power flow sharing between the sources with the aim of satisfying the requested power while declining the fuel consumption and enhancing the system's lifetime. Finally, the best-achieved size of each architecture is compared in terms of trip cost, capital cost, and the system weight. The obtained results show that passive topology can reduce the trip cost by 14.8% and 6.4% compared to full-active and semi-active ones, respectively. However, the active architecture results in less degradation in the FC compared to the other two topologies. Furthermore, a validation phase is done under a real driving profile and the results are further discussed.

1. Introduction

The transportation sector is one of the main contributors to the emission of greenhouse gases owing to its dependency on fossil fuels [1, 2]. However, green vehicles and fuels are creating the necessary bases to decarbonize this sector while enhancing utilities to consumers and the broader economy [3]. The cleaner solutions are based on the electrification of the powertrain through mild/full/plug-in hybrid electric vehicle (HEV), battery electric vehicle (BEV), and fuel cell electric vehicle (FCEV) technologies [4]. Among these solutions, FCEV is one of the most promising due to zero-local emissions, long driving range, and fast refueling [5]. In the short term, the fuel cell (FC) technology will be expensive due to the high capital cost of refilling stations, tanks, and FC systems [6]. However, the FC cost is expected to become competitive with the internal combustion engine (ICE) by 2025, according to the performed study in [7]. One of the weaknesses of the FC systems is nonetheless their sensitivity to the abrupt load fluctuations which are common in vehicular application [8]. These rapid changes, which can be due to vehicle acceleration, lead to a marked decline in oxygen concentration and consequently a sharp power drop in the FC system [9, 10]. Consequently, they are unfavorable for the lifetime of the FC stack as they cause a reduction in the mass activity and an increment on the internal electrical resistance [11, 12]. To address these concerns, the hybridization of the FC system with an energy storage system (ESS), such as battery or supercapacitor (SC) has been broadly practiced [13]. This hybridization not only resolves the discussed issues, but also offers the ability to capture regenerative braking energy (since FC stack cannot absorb the energy), increase fuel economy, and deliver a more flexible operating strategy. Various architectures for hybridizing a FC system have been developed in the literature. These architectures fit into two categories of active and passive [14]. Active configuration is denoted by the association of the power source to the DC bus through a DC-DC converter. It is divided into

two groups of semi-active, where only one of the sources is interfaced by a converter, and full-active, where each of the sources has their own converters. Active topology is a common choice in the literature as it has the flexibility to actively control the power split between the FC stack and the ESS and enhance the lifetime of the system. This topology has been applied more in high-duty applications, such as tramway, hybrid bus, ships, and excavators [15-18]. In these applications, the voltage at the DC bus should be stable and within a specific range as the motor drive and the auxiliary systems are usually coupled directly to the DC bus. In the semi-active category, the FC is normally connected to the DC bus via a DC/DC converter while the ESS is directly connected there. This configuration is extensively used because the passive component absorbs the surplus energy in the bus, which facilitates the power split control over the FC. Its main application is in light-duty vehicles, such as Toyota Mirai, Honda Clarity, among others [19]. Regarding the passive configuration, all the components are directly connected to the DC bus in a parallel manner. Compared to the previous topologies, it benefits from a structure with fewer components and simpler implementation.

Concerning the power split, in active topologies they are typically performed through the formulation of an energy management strategy (EMS) [20, 21]. In this respect, some works tend to operate the FC in a maximum efficiency region in order to improve the system performance and efficiency [22-24]. While an active configuration offers a well-defined power split among the sources, some studies have proposed the employment of passive architectures since they can decline the complexity, cost, and weight of the vehicle [25, 26]. Passive topology is highly straightforward and has a self-management due to the characteristics (different impedance) of the sources. In other words, it does not require an EMS to perform the power distribution between the sources [27]. However, this can lead to the presence of high power ripples at the FC side and consequently increase the degradation rate of the stack.

In [28], a comparison of active and passive hybrid topologies for a FC-battery vehicle indicates that as long as the requested power does not contain high fluctuations, the passive topology has a superior performance. However, as the requested power starts having high-pulses, the FC stack operation is shifted to the low-efficiency regions. The active and passive topology selection between a SC and a battery pack, as the complementary power source in a FC hybrid electric vehicle (FCHEV), has been studied in [29]. This study shows that the use of an active topology with a battery results in noticeable power changes in the FC stack compared to the passive configuration of FC and SC. The use of a SC as the ESS stems from the fact that the passive coupling of a FC stack with a SC bank is more prevalent than a battery pack since the SC characteristics are more suitable for coping with the intermittency of behavior in a FCHEV with such a configuration. The passive topology with SC makes the drawn power from the FC smoother and leads to a higher energetic efficiency and longer lifetime of the FC. In addition, SC benefits from a high power density, high efficiency (in high voltage region), fast charge, wide operating temperature range, and excellent recyclability [30]. Regarding the FC-SC active configurations, several EMSs are proposed for distributing the power between the FC stack and the SC bank. The common concerns in all these works, using the full-active topology, are to compensate for the slow dynamic of the FC stack, minimize the hydrogen consumption, and increase the efficiency while taking care of the lifetime of the vehicle [31-33]. In [34, 35], two state machine controls based on equivalent consumption minimization for FC-SC full-active configuration are implemented to power up a tramway. Both methods identify the optimum FC operating range, and the optimization of the power distribution based on different situations at each timestep. In [36], a semi-active FC-SC topology is utilized in which the SC is directly connected to the DC bus and the FC is interfaced with a unidirectional converter. The SC supplies and passively absorbs the peak power, and the FC is regulated by an EMS based on game theory, which considers the controller and the future driving condition to reduce hydrogen consumption and avoid unnecessary on-off cycles. In [37, 38], the principal objective is the passive hybridization of a SC to a single FC. The attained experimental

outcomes show that the passive topology avoids negative voltage, has self-protection in sudden power fluctuations, and improves the energetic performance as patented by NISSAN company [39]. In [40], a 9.5-kW proton exchange membrane FC (PEMFC) is connected to a SC bank by a passive architecture. This configuration has decreased the dynamic load, idling time, and rapid load changes in the FC without using a DC-DC converter.

Based on the previously discussed articles, a SWOT analysis is performed to recognize the most suitable configuration for a hybrid FC recreational vehicle. In this respect, the internal origin factors are the ones that are part of the architecture, and the external origin factors are the ones that cannot be directly controlled. This decision-making tool, shown in Fig. 1, is represented in a matrix of four quadrants; Strengths, Weakness, Opportunities, and Threats. The strengths are the characteristics that pin out each configuration, the weaknesses are the inherent disadvantages, the opportunities are the elements in the environment that can give value to the configuration, and the threats are external circumstances that can cause problems for implementing a configuration [41].

		Helpful	Harmful
		Strengths	Weakness
Internal origin	Full-active	• Complete system control • Lowest fuel consumption	• Complicated control system • Highest capital cost
	Semi-active	• Good system management • No unnecessary on-off cycles	• Heavy and voluminous systems • Higher fuel consumption
		• Low-pass filter operation	• The ESS will degrade faster
	Passive	• Low mass and volume requirements	• No control over current distribution
		Opportunities	Threats
External origin	Full-active	• Stable DC bus voltage level	• Converter deals with high current peaks
	Semi-active	• Large variety of EMS • Coupling small component size with converter	• The possible fault of the system caused by the converter
		• High industrial acceptance	• The DC bus voltage range will shrink while the ESS degrades
	Passive	• Low electric losses conversion	• The initial voltage of the ESS should be in the range

Fig. 1. SWOT analysis of hybrid configurations

After taking into consideration the previous literature study, the first hypothesis regarding the recreational vehicle case study of this work is that passive configuration is a suitable candidate solution. It stems from the fact that recreational vehicles are limited in terms of mass and volume. Moreover, these vehicles present more erratic and aggressive speed profiles. Under such a basis, a passive configuration is a more compact power supply system with the self-coordination of each component. The second hypothesis is that the configurations with an active coupling will have a longer operational time, because they avoid operating in high degradation conditions. The third hypothesis is the use of SC as an ESS. This is due to its resilience and high-power density. In this sense, the SC operates as a low-pass filter that leaves the main components of the requested power to the FC system to supply. In this respect, this work aims to investigate the applicability of hybrid passive FC configuration for a recreational vehicle.

In view of the reviewed papers, some efforts have already been made concerning the use of active and passive FC-SC topologies in vehicular applications. However, so far, these configurations have not been benchmarked comprehensively. Most studies utilize the same size of FC-SC for active and passive configurations while a customized size is required for each of them to exploit their strengths and have a fair comparison. In addition to common concerns regarding the cost, hydrogen consumption, lifetime of the system, lightness, and compactness are also necessary considerations in the design of this sort of vehicle. In order to bridge the mentioned gaps and validate the hypothesis, this article presents a benchmark study of three FC-SC hybrid energy system configurations, namely full-active, semi-active, and passive. The main objective of this article is to comprehensively weigh up the pros and cons of each customized configuration, in terms of hydrogen consumption, FC degradation, and system weight. In order to reach a fair comparison, an optimal EMS based on dynamic programming (DP) is used because the sizing and the power split methods are intrinsically related to the performance and cost of the power supply system. The rest

of this paper is organized as follows. In section 2, the modeling of the vehicle powertrain along with the SC and FC is presented using some semi-empirical equations. Section 3 deals with the component sizing by using genetic algorithm (GA) while applying DP to do the power split for the active topologies. Section 4 represents a rigorous comparison of the developed topologies under a standard and a real on-road driving profile. Finally, the conclusion is given in section 5.

2. Hybrid electric vehicle modeling

The investigated vehicle in this manuscript (e-TESC-3W platform) is a three-wheel pure electric vehicle specifically employed for recreational purposes, presented in Fig. 2(a). These types of vehicles are normally exposed to high dynamics and need to be light and compact. Given these characteristics, the sizing of the components becomes a critical stage that directly influences the performance, cost, and dimensions of the vehicle. The performed study in [42] shows that a FCHEV can have a similar weight to the commercially available motorcycles which are propelled by an ICE. Moreover, its tank-to-wheel consumed energy is less than an ICE.

The studied e-TESC-3W platform comprises a permanent magnet synchronous motor (28 kW and 96 V) directly connected to the rear wheel and utilized as an experimental test rig in e-TESC laboratory at the University of Sherbrooke [43-45]. The motor speed is regulated with a three-phase power inverter that converts the direct current in the bus to alternate current. The main characteristics of this vehicle are summarized in Table 1 and explained thoroughly in [44].

Table 1: Vehicle specifications

Variable	Symbol	Value	Units
Vehicle mass (w/o power source)	m_{eq}	350	kg
Typical rolling resistance coefficient	μ_{fr}	0.02	-
Typical aerodynamic drag coefficient	C_d	0.75	-
Vehicle front area	A_{aero}	1.25	m2
Wheel radius	r	0.305	m
Belt transmission drive ratio	G_{gb}	5.033 (30:151)	-
Belt transmission drive efficiency	η_{gb}	95	%

Maximum vehicle speed	$V_{EV,max}$	140	km/ h-1
Operating motor driver voltage	u_{DC}	80 - 120	V

The focus of this work is to compare the performance of this platform for active, semi-active, and passive topologies of FC-SC. Hereinafter, the modeling process of active and passive configurations are discussed with the help of energetic macroscopic representation (EMR). EMR is a graphical formalism of complex multiphysics systems that shows the energetic properties of the elements and their interactions [46]. In addition, a control loop can be easily deduced based on an inversion of the system model.

2.1. Traction system

The traction system of this vehicle is represented using a static model (efficiency map lookup table) of the electric machine and power electronics. This model is composed of different forces and Newton's second law of motion. Fig. 2(b) shows the EMR of the traction system, in which the driving cycle is the reference variable of the control loop, and the torque of the electric motor is the control action [43]. The power source devices are represented as source elements, in which the requested current of the traction system is the input and the voltage on the DC bus is the output. The vehicle modeling is represented by the following equations (1-8):
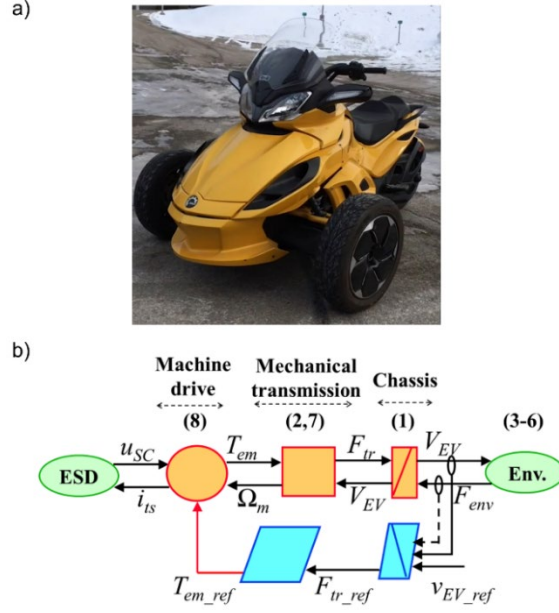
a)

b)

Machine drive (8) Mechanical transmission (2,7) Chassis (1) (3-6)

u_{SC} T_{em} F_{tr} V_{EV}

ESD i_{ts} Ω_m V_{EV} F_{env} Env.

T_{em_ref} F_{tr_ref} v_{EV_ref}

Fig. 2. e-TESC 3W electric vehicle platform, a) picture and, b) the traction system model

$$\frac{dV_{EV}}{dt} = \frac{(F_{tr} - F_{env})}{m_{eq}} \tag{1}$$

$$F_{tr} = (G_{gb}/r)T_{em}\eta_{gb}^{\beta} \tag{2}$$

$$F_{env} = F_{roll} + F_{grade} + F_{air} \tag{3}$$

$$F_{roll} = m_{eq}g\mu_{fr}\cos\theta \tag{4}$$

$$F_{air} = 0.5\rho_{air}A_{aero}C_d V_{EV}^2 \tag{5}$$

$$F_{grade} = m_{eq}g\sin\theta \tag{6}$$

$$\Omega_m = (G_{gb}/r)V_{EV} \tag{7}$$

where F_{tr} is the traction force, F_{env} is the vehicle traction force resistance, m_{eq} is the vehicle mass, G_{gb} is the gearbox transmission ratio, r is the wheel radius, T_{em} is the electric machine torque, η_{gb} is the gearbox transmission efficiency, ρ_{air} is the air density (1.2 kg/m^3), β is a discrete value that takes the value of -1 when the vehicle is in braking mode otherwise it is 1, and Ω_m is the rotor

rotation speed. It is assumed that the reference torque $T_{em,r}$ is the same as the measured one. Where the employs coefficient, rolling resistance μ_{fr} and aerodynamic drag C_d, are typical values. The vehicle's mathematical model has been validated with an on-road driving test carried out in the e-TESC laboratory [45], which is considered adequate for the benchmark analysis purpose of this paper..

Therefore, the necessary current of the electric motor to achieve the reference torque $T_{em,r}$ is then calculated by:

$$i_{ts} = \left(T_{em}\Omega_m\eta_m^\beta\right)/u_{DC} \tag{8}$$

where u_{DC} is the voltage on the DC bus, and η_m is the drive efficiency that considers the inverter and motor efficiency. This voltage corresponds to the voltage of the SC in the passive and semi-active configurations. In the full-active configuration, it corresponds to the nominal voltage of the motor, which is the interconnection of the two DC-DC converters.

2.2. Fuel cell system

The FC system is represented by an electrochemical based PEMFC model proposed by Amphlett et al. studied in several works [47, 48]. This model represents the performance of the FC by a function that includes the reversible potential, which is the maximum possible voltage of the FC, and the irreversible voltage losses. Moreover, this data-driven model has a low computational cost and a good interpolation an extrapolation approximation [49]. The selected FC system for this work is the FCvelocity-9SSL from Ballard Power Systems, whose size varies from 3.8 kW to 27.3kW [50]. The PEMFC voltage (u_{FC}) is approximated by the following equations (9-13):

$$u_{FC} = N_{FC}(E_{Nernst} + u_{act} + u_{ohmic} + u_{con}) \tag{9}$$

$$E_{Nernst} = 1.229 - 0.85 \times 10^{-3}(T_{FC} - 298.15) + 4.3085 \times 10^{-5}T_{FC}[\ln(p_{H2}) + 0.5\ln(p_{O2})] \tag{10}$$

$$\begin{cases} u_{act} = \xi_1 + \xi_2 T_{FC} + \xi_3 T_{FC} ln(CO_2) + \xi_4 T_{FC} ln(i_{FC}) \\ C_{O_2}^* = \dfrac{P_{O2}}{5.08 \times 10^6 \ exp(-498/T_{FC})} \end{cases} \tag{11}$$

$$u_{ohmic} = -i_{FC} R_{internal} = -i_{FC}(\zeta_1 + \zeta_2 T_{FC} + \zeta_3 i_{FC}) \tag{12}$$

$$u_{con} = \alpha ln(1 - i_{FC}/i_{FC,max}) \tag{13}$$

where N_{FC} is the number of cells, E_{Nernst} is the reversible voltage, u_{act} is the activation loss, u_{ohmic} is the ohmic loss, u_{con} is the concentration loss, T_{FC} is the stack temperature, p_{H2} is the hydrogen partial pressure, p_{O2} is the oxygen partial pressure, ξ_n (n = 1 … 4) is the empirical coefficients, $C_{O_2}^*$ is the oxygen concentration, i_{FC} is the FC operating current, $R_{internal}$ is the internal resistor defined by the three parametric coefficients ζ_n (n = 1 … 3), α is a semi-empirical parameter related to the diffusion mechanism ($0.3 \leq \alpha \leq 1.8$), and $i_{FC,max}$ is the maximum current. The Amphlett voltage model is compared with the single cell voltage values reported in the Ballard datasheet, shown in Fig. 3(a). The polarization curve represents the FC voltage output for a given current load.

The oxygen partial pressure is approximated as 21% of the cathode pressure since it is the percentage of oxygen in the air flowing to the cathode. Regarding the hydrogen partial pressure, it is approximated as 99% of the anode pressure. The cathode pressure is calculated by (14) in terms of current since the airflow mainly depends on the current. This equation has been introduced in [51], as fitted to experimental data under different current levels, and the anode inlet pressure p_{an} has been maintained at 0.2 bar above the cathode pressure p_{ca}. This is to reduce the nitrogen crossover, enhance the cell stability, and evacuate the hydrogen in form of water through the cathode in case of an internal leak.

$$p_{ca} = a_1 + a_2 i_{FC} + a_3 i_{FC}{}^2 + a_4 i_{FC}{}^3 \tag{14}$$

The thermal behavior of the FC is described by using the law of conservation of energy, as shown in the Fig. 3(b). The energy balance for describing the temperature dynamic of the FC system is explained in [52], by considering only the heat dissipated by the liquid cooling system.

$$Q_{heat} = N_{FC} i_{FC} (1.254 - u_{FC}) \tag{15}$$

$$Q_{conv} = H_{FC} (T_{FC} - T_{amb}) \tag{16}$$

$$\frac{dT_{FC}}{dt} = \frac{Q_{heat} - Q_{conv}}{MC_{FC}} \tag{17}$$

where the generated heat in the FC Q_{heat} is the residual energy of the ideal potential minus the real potential, H_{FC} is the heat transfer coefficient under free convection defined experimentally in [53], the heat transfer coefficient is calculated by k_{t1} and k_{t2} which are empirical coefficients obtained experimentally in [52], T_{amb} is the ambient temperature, T_{FC} is the stack temperature, Q_{conv} is the heat dissipated due to convection, and MC_{FC} is the thermal capacity of the FC. After considering all the losses from the auxiliary systems, the power of the FC system is calculated as follow:

$$P_{FC,aux} = P_{comp} + P_{fan} \tag{18}$$

$$P_{comp} = \frac{1}{\eta_{comp}} W_{air} c_p T_{amb} \left(\frac{p_{ca}}{p_{amb}}^{\gamma-1/\gamma} - 1 \right) \tag{19}$$

$$P_{FC} = u_{FC} i_{FC} \tag{20}$$

$$W_{air} = \lambda W_{O_2} / x_{O_2} \tag{21}$$

$$W_{O_2} = M_{O_2} N_{FC} i_{FC} / 2F \tag{22}$$

$$P_{FC,sys} = P_{FC} - P_{FC,aux} \tag{23}$$

where $P_{FC,aux}$ is composed of the the cooling system losses which are the fan power (P_{fan}) that is considered constant (200W) and the power of the compressor P_{comp}. The efficiency of the

compressor η_{comp} is estimated as 70% [54], W_{air} represents the rate of the consumed air, c_p is the specific heat capacity of air (1005 J/Kg), p_{amb} is the ambient pressure, γ is the specific heat ratio of the air (1.4), λ is the oxygen excess ratio constant (2), W_{O_2} is the rate of oxygen consumed through the cathode, x_{O_2} is the ideal oxygen mass fraction in the air (23.3%), M_{O_2} is the oxygen molar mass (32 gr/mol), and F is the Faraday constant. Finally, the $P_{FC,sys}$ is the power of the FC system after the auxiliary losses.
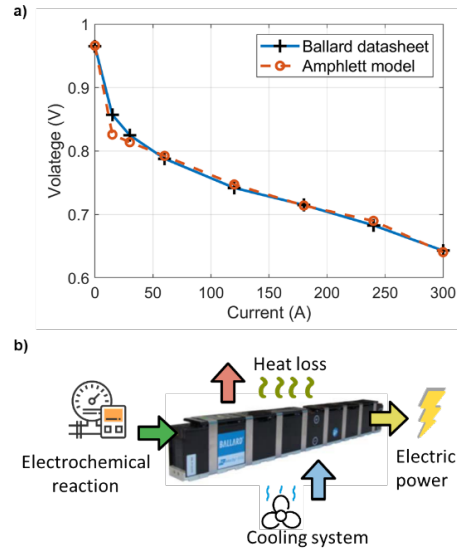

Fig. 3. Studied FC stack from Ballard Power Systems, a) FC voltage model comparison for a single cell, b) energy balance representation.

The efficiency of the system is calculated considering the consumed energy by the liquid and air-cooling system.

$$\eta_{FC} = \left(i_{FC,sys} u_{FC} \right) / \left(W_{H_2} \times HHV \right) \tag{23}$$

$$W_{H_2} = 0.00696 i_{FC} N_{FC} \tag{24}$$

where HHV is the hydrogen high heating value [55], and W_{H_2} is the hydrogen flow consumed in terms of the current across the FC.

2.3. Supercapacitor and DC-DC converter

The SC is represented by an equivalent circuit model that corresponds to the electrical Faradic reaction that occurred in the electrode surface. In [56], a comparative study of five equivalent circuit models is performed under different operational temperatures. Based on the reported error and ease of implementation, a classical RC model has been selected. The electrical behavior is calculated as follow:

$$u_{SC}(t) = u_c(0) + \frac{1}{C_{SC}} \int i_{SC} dt - i_{SC} R_{SC} \tag{25}$$

where $u_c(0)$ is the initial open-circuit voltage (OCV) of the capacitance element, i_{SC} is the current across the SC, C_{SC} is the equivalent capacitance value of the SC, and R_{SC} is the equivalent resistor value of the SC. The utilized SC of this work is based on Maxwell Technologies, and the equivalent capacitance and resistor for each model are provided in the manufacturer datasheet [57]. The validation of this equivalent circuit model has already been done in previous papers [58].

The remaining energy in the SC is estimated by the formula of Coulomb counting [59].

$$SOC_{SC}(t) = SOC_{SC}(0) + \int \frac{i_{SC} \, dt}{Q_{max}} \tag{26}$$

where $SOC_{SC}(0)$ represents the initial level of charge, and Q_{max} is the maximum available capacity.

For the active coupling, a DC-DC converter is required to boost the voltage level of the FC or the SC. This is a common technique used in commercial vehicles, such as Toyota Mirai [60]. In the developed simulator, the DC-DC converter is considered as an efficiency ratio, which is multiplied by the power of the active device [61]. In the case of the FC system, its effective power in the DC bus is calculated as follow:

$$P_{FC,bus} = P_{FC,sys} * DC_{eff} \tag{27}$$

3. Problem definition and two-level optimization

In the literature, different types of FC hybrid architectures are proposed based on the selected application [62]. The hybrid configurations studied in this work are full-active, semi-active, and passive, as shown in Fig. 4. Fig.4(a) represents the full-active configuration. In this structure, the FC and SC are connected to the DC bus via a DC-DC converter. This configuration benefits from a flexible power control between the FC and SC, and a more stable voltage level in the DC bus. However, to provide the demanded power, complicated and strict control techniques are required. Fig.4(b) is the semi-active configuration, in which the FC is connected through a DC-DC converter to the DC bus and the SC is directly connected. In this configuration, the SC voltage represents the DC bus voltage, so the EMS must regulate the level of charge of the SC. The last structure, passive configuration, is shown in Fig.4(c). In this topology, FC and SC are directly connected to the DC bus. To avoid reverse current inside the FC, a diode is placed in series with it. This configuration does not require an EMS, and the power splitting depends on the natural behavior of each component. Most of the performed studies on this structure have concentrated on the sizing method because it is the principal factor that influences the performance of the system. The FC current is always positive and is defined as follows:

$$i_{FC} = \frac{u_{FC} - u_{SC}}{R_D} \tag{27}$$

where R_D is the equivalent diode resistance. It can be implied from the passive structure that the voltage of the FC tends to have the same level as the SC voltage, and the requested current is equal to the sum of FC and SC currents.
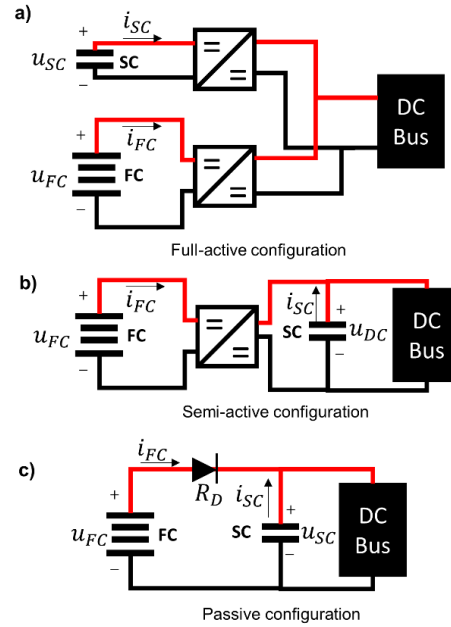
Fig. 4. Studied configurations, a) full-active, b) semi-active, and c) passive.

In the case of full-active and semi-active configurations, a two-step optimization method is used to define the best system size and power split [63, 64]. The simultaneous optimization-based energy management and component sizing methods have been successfully implemented in previous works [65, 66]. This is a plant/controller iterative optimization that consists of two nested optimization loops. The first step optimizes the cost function by searching the plant variables that are the set of parameters for the system size. The second step is in charge of the optimization of the controller design for each proposed plant [67]. As shown in Fig. 5, the first step is a metaheuristic method used to define the FC and SC sizes. The second step is an inner loop, where DP splits the power between the components while minimizing a cost function. In the passive configuration, only the metaheuristic method is applied since there is no control over the sources.
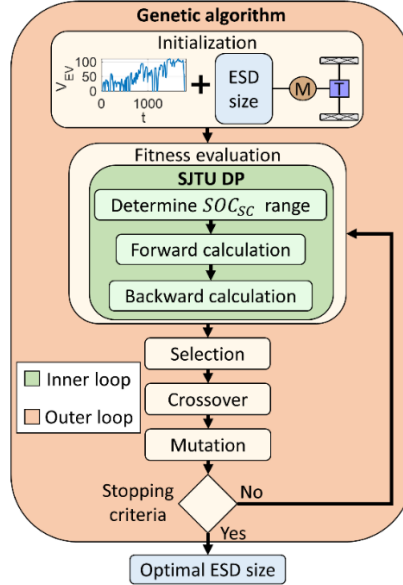
Fig. 5. The framework of the two-step optimization for sizing and EMS

3.1. System cost and durability

Although cost is a major obstacle for the commercialization of fuel-cell vehicles, most of the existing EMSs have only focused on the minimization of the hydrogen consumption [68, 69]. Only a few papers have tried to maximize the overall FC system efficiency while extending its lifetime and avoiding harmful FC conditions [65, 70-72]. In this respect, in this work, a multi-objective optimization problem is utilized to minimize hydrogen consumption as well as the system degradation. This problem is solved by using a weighted-sum approach, in which the importance of each objective is defined by a cost factor [73]. In the market, the price of the components varies based on the number of units to buy and manufacturer. For this reason, the standard price proposed by the US Department of Energy (DoE) is used in this work and summarized in Table 2.

Table 2: System cost breakdown

Component	Cost	Variable	Ref.
FC system	40 $/kW_{net}$	$\$FC_{sys}$	[74]
SC	15 $/Wh	$\$SC$	[75]
DC-DC converter	50 $/kW$	$\$DC_{conv}$	[76]
Hydrogen	2.3 $/kg\ H_2$	$\$H_2$	[77]

The trip cost is in terms of USD and is composed of the consumed hydrogen and a fraction of the system cost. The FC cost is linked to the system degradation, which is considered as the percentage of reduction in the maximum power. The US DoE has defined the FC end of life (EOL) as a 10% drop in the maximum power, and an operational objective of 5000 hours [74]. However, the SC and DC-DC converter in normal conditions have an expected lifetime in terms of thousands of cycles [78]. To increase the importance of the SC and DC-DC converter in the optimization process, their costs are linked to the trip time. The proposed trip cost used in the optimization process is calculated as follow:

$$\$Trip = \$FC_{sys}\Delta_{FC} + \$H_2 \int W_{H_2}\text{dt} + \$SC\Delta_{trip} + \$DC_{conv}\Delta_{trip} \tag{28}$$

where Δ_{FC} represents the percentage of degradation in the FC system along the trip, the total consumed hydrogen is calculated by the integration of the hydrogen flow (W_{H_2}), and Δ_{trip} is the trip time divided by the operational objective of 5000 hours.

The major causes of degradation in a FC system are the high and low power, the start-stop cycles, the fast-dynamic loads, and the natural decay [79]. Table 3 summarizes the empirical coefficients of FC performance degradation in terms of percentage [80].

Table 3: Coefficients of FC performance degradation.

Variable	Coefficient
k_1	0.00126 (%/h)
k_2	0.00196 (%/cycle)
k_3	5.93×10^{-5} (%/cycle)
k_4	0.00147 (%/h)
k_5	0.002 (%/h)

The percentage of FC degradation is calculated as the sum of FC degradation under each condition.

$$\Delta_{FC} = k_1 t_1 + k_2 n_1 + k_3 n_2 + k_4 t_2 + k_5 t_{FC_{ON}} \tag{29}$$

where k_1 is the low power coefficient (less than 5% of maximum power), k_2 represents one start-stop coefficient, k_3 is the fast-dynamics coefficient (absolute value of power variations larger than 10% of maximum power per second), k_4 is the high power coefficient (more than 90% of maximum power), k_5 is the natural decay rate (the time that FC is under operation), t_i $(1,2,FC_{ON})$ are the operational time in their corresponding conditions. In addition, system constrains are implemented to guarantee that the system works within the defined operating conditions.

3.2. Dynamic programming

The new unified DP model and its solution method (SJTU DP), proposed in [81, 82], is implemented in this work to do the energy management of the full-active and semi-active configurations. This method solves the main four problems of DP, namely the dimension disaster, standardization, Markov problem, and interpolation leakage. The main characteristics of this method are the state-space model with four state variables, the multi-objective cost function formulation, the dimension reduction calculation method, and the forward-backward calculation sequence. Compared with Basic DP and Level-Set DP, the utilized method shows less computational time and better calculation accuracy.

The unified state-space equation of DP model for full-active and semi-active configurations is represented by four states.

$$
\begin{cases}
SOC_{SC}(k+1) = SOC_{SC}(k) + \int \dfrac{i_{SC}(k)\,dk}{Q_{max}} \\
u_{SC}(k+1) = u_c(k) + \dfrac{1}{C_{SC}} \int i_{SC}(k)dk - i_{SC}(k)R_{SC} \\
P_{FC,s}(k+1) = u_{FC}(k) * i_{FC}(k) \\
M(k+1) = \psi\big(P_{FC,s}, FC_s, k\big)
\end{cases}
\tag{30}
$$

where the state variable vector is $x = \big[SOC_{SC}, u_{SC}, P_{FC,s}, M\big]$, $P_{FC,s}$ represents the power of the FC as a state variable while i_{FC} is the current of the FC as a control variable. In addition, an operational work mode M is included in the states to reduce the extra calculation that will end in infeasible

conditions. This work mode is defined by the function $\psi(P_{FC,s}, FC_s, k)$ that creates a relationship between the work mode, the control variable, and the FC state FC_s. The work mode can take four discrete values: SC mode (SCM), Start mode (SM), Normal work mode (NWM), Shutdown mode (SDM). The SCM is defined as the stage when the FC is off and all the requested power is supplied by the SC. SM represents the turning on the procedure of the FC until the FC reaches the minimum idle current level ($i_{FC,idle}$). During the NWM, the requested power is supplied by both FC and SC, which are active, and OM is the turn-off procedure of the FC. The system can change from one mode to another by respecting a fixed order (SCM-SM-NWM-SDM-SCM). That means the FC cannot switch-off while it is starting up. By doing so, the number of unnecessary turn-on cycles is reduced.

In order to assure that the system operates in the desired conditions, some limitations need to be satisfied. They are represented by the following constraints.

$$\begin{cases} SOC_{SC,min} \leq SOC_{SC} \leq SOC_{SC,max} \\ i_{FC,min} \leq i_{FC} \leq i_{FC,max} \\ i_{SC,min} \leq i_{SC} \leq i_{SC,max} \\ u_{DC,min} \leq u_{DC} \leq u_{DC,max} \\ \Delta P_{FC,min} \leq \Delta P_{FC} \leq \Delta P_{FC,max} \end{cases} \tag{31}$$

where the SOC_{SC} range is selected based on typical values found in the literature, the current limits are established by the manufacturer, the u_{DC} range is determined based on the motor driver operating voltage, and the ΔP_{FC} is the slew rate of the FC power and can be calculated by:

$$\Delta P_{FC} = P_{FC}(k) - P_{FC,s}(k) \tag{32}$$

The main objective of DP is to minimize the trip cost specified in (28) by finding the right FC current while respecting the constraints in (31). The trip cost equation is a function that only depends on the current state and the control variable at that step k_{th}. This proves that the DP model fulfills the requirement of the Markov characteristics of DP. The SJTU DP solution method consists mainly in three steps: first, calculating the boundary range of the state variable with the maximum

and minimum power for each k_{th} step. Secondly, a forward calculation to determine the minimum cost of each grid point while respecting the constraints. Lastly, defining the optimal control sequence backward.

Table 4 summarizes the constraints utilized in this work in order to warranty that the proposed plants will meet the system requirements. Moreover, these parameters have been selected to reduce the degradation, and maximize the performance of the power sources [83-87].

Table 4: Optimization parameters and constrains of DP method

Parameter	Min	Max
i_{FC}	0 A	300 A
i_{SC}	-300 A	300 A
SOC_{SC}	50 %	90 %
u_{DC}	80 V	120 V
$\Delta P_{FC,min}$	$-0.1P_{FC,max}$	$0.1P_{FC,max}$

3.3. Metaheuristic sizing

The optimization of the sizing process in hybrid systems implies non-monotonic effects on objectives and constraints to be reached, while it tries not to get trapped in local optimums [88]. As shown in Fig. 5, GA is implemented to define the optimal size of the power sources in a way to minimize the trip cost. GA is a derivative-free metaheuristic method capable of solving the non-linear constrained optimization problem of the energy system component design. GA is inspired by the process of natural selection described in Darwin's theory of evolution. This optimization technique operates by encoding potential solutions as simple chromosome-like data structures and then applies genetic operators to those structures, such as mutation, crossover, and survival of the fittest. Over many iterations, its population of chromosomes evolves toward better solutions. The algorithm typically terminates when the diversity of its population reaches a predetermined minimum, or a maximum number of iterations [89].

The parameters to be optimized by GA in this work are defined as $x = [N_{FC}, C_{SC,u}, N_{SC,s}, N_{SC,p}]$ where x is the optimized vector, N_{FC} represents the number of cells of the FC stack, $C_{SC,u}$ is the capacitance of a single SC, $N_{SC,s}$ indicates the number of SC connected in series, and $N_{SC,p}$ specifies the number of parallel series banks of SC. The number of generations is set to 100, the population size is 150, the elite count is 10, and the crossover fraction is 0.8. These settings cause GA to use a larger population, to expect the best solution to be close in the initial random population, and to keep searching in the design space until its best member fitness changes by a small amount.

The targeted parameters for optimization by GA are defined as discrete values based on the commercial capacitance of Maxwell SC and the size of the Ballard FC [50, 57]. Table 5 summarizes the optimization space of the plant.

Table 5: The range of the targeted parameters for optimization

Variable	Bounded range
N_{FC}	[55,71,75,80,90,110,115,135]
$C_{SC,u}$	[100,150,310,325,350,360,450,650,1200,1500,2000,3000,3400]
$N_{SC,s}$	$\in Z \geq 1, \leq 60$
$N_{SC,p}$	$\in Z \geq 1, \leq 60$

4. Results analysis

In this work, the standard World Motorcycle Test Cycle (WMTC) is utilized for the optimal sizing procedure. WMTC represents the collection and analysis of daily motorcycle driving behavior in Europe, Japan, and the USA [90]. It is composed of three regimes: urban traffic, slow country-road, and fast country-roads. The fitness function convergence trend of the optimal based sizing method for the three FC-SC configurations is shown in Fig. 6. The trend of mean value alteration represents

all different sizes that fulfil the system requirement, and the combination with the lowest cost function value of each population is recorded in the best fitness curve. The minimization trend of the best fitness value has become almost stable after 20 iterations in the full-active, and after 50 iterations in semi-active and passive configurations. Moreover, the mean value trend converges for all the configurations at the end, showing that the best fitness value is the global/near-global optimal result.
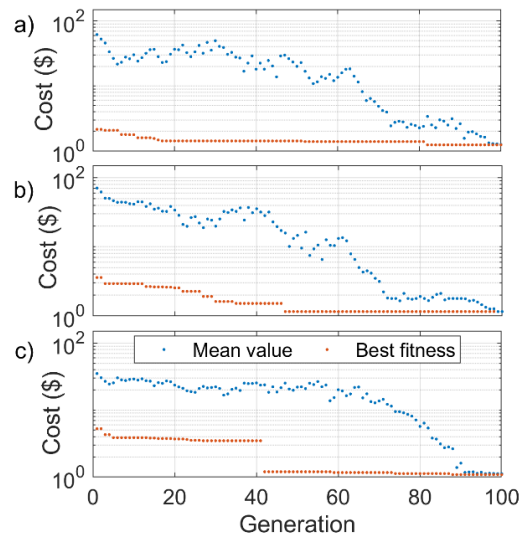

Fig. 6. Fitness function minimization trend for: a) full-active, b) semi-active, and c) passive configurations.

The results of the optimization process are summarized in Table 6, where the FC and SC size, mass and cost are reported. It should be noted that the system mass and volume are obtained from the datasheets and it shows an approximated value of the power supply system. The full-active configuration is the one with the smallest capacitance value, followed by the semi-active. The passive configuration is the one with the biggest FC size and higher SC capacity. On the other hand, passive configuration, which does not use any DC-DC converters, benefits from a light mass and low volume.

Table 6. Obtained results by the two-step optimization method

Configuration	$C_{SC,u}$	$R_{SC,u}$	Q_{max}	$N_{SC,s}$	$N_{SC,p}$	$P_{FC,max}$	System mass	Capital cost
Full-active	310 F	2.2 mΩ	202 Wh	43	15	22.2 kW	77.9 kg	$ 6424.00
Semi-active	310 F	2.2 mΩ	230 Wh	49	15	22.2 kW	72.3 kg	$ 5598.00
Passive	450 F	2.8 mΩ	241 Wh	59	9	27.3 kW	59.3 kg	$ 4721.00

The requested power (P_{req}), the effective power of the FC system in the DC bus ($P_{FC,bus}$), and the power in the SC (P_{SC}) for the FC-SC configurations are shown in Fig. 7. As shown in Fig. 7(a), the first part of the WMTC profile starts with a cold start and consists of eight micro-trips with a maximum speed of 60 km/h. The second part contains two micro-trips with a maximum speed of 95 km/h. The third part is one micro-trip with the top speed at 110 km/h. As presented in Fig. 7(c), semi-active configuration operates the FC in more stable steps, but the SC manages to absorb all the power peaks. Therefore, the regulation of active configuration reduces those peaks and makes the operation possible with a smaller number of SCs. Also, it is observed that semi-active and full-active configurations operate in SCM around 50 seconds in the beginning. Regarding the passive configuration shown in Fig. 5(d), the SC works as a low pass filter, and the FC follows the low frequency and main components of the requested power. In addition, it is observed that the FC voltage tends to follow the SC voltage level, as described in equation (27), until it reaches its OCV.
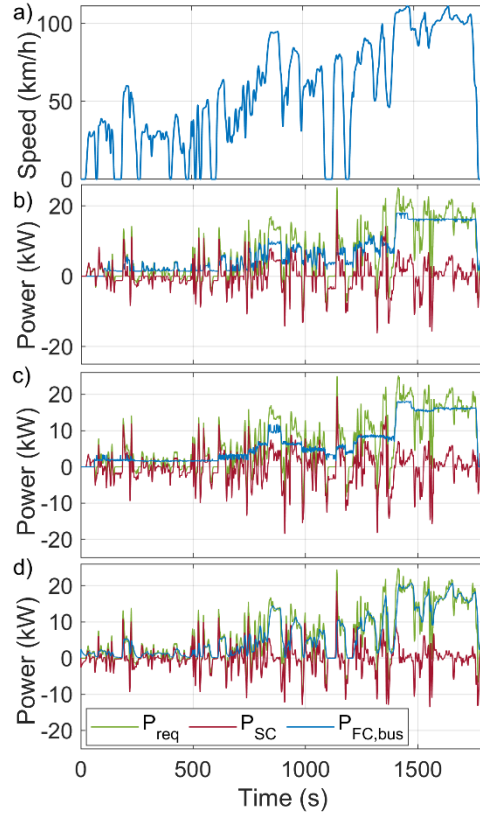
Fig. 7. Power split of WMTC profile by the two-step optimization method, a) utilized WMTC driving cycle, b) full-active, c) semi-active, d) passive configuration.

The results of the best fitness function are presented in Table 7. According to Table 7, the passive configuration has achieved the lowest value in terms of trip cost compared to other configurations. However, full-active, and semi-active operate the FC in a way to minimize its degradation. This superior performance of the passive configuration is achieved mainly due to not using a DC-DC converter. This reduces the cost and energy losses and generates a lower hydrogen consumption.

Table 7. Breakdown of the trip cost for WMTC profile

Configuration	H_2 cons.	FC deg.	SC cost	Conv. cost	$Trip
Full-active	$ 0.45	$ 0.25	$ 0.30	$ 0.24	$ 1.24
Semi-active	$ 0.43	$ 0.26	$ 0.35	$ 0.12	$ 1.15
Passive	$ 0.38	$ 0.34	$ 0.36	-	$ 1.08

The current distribution analysis is shown in Fig. 8. Fig. 8(a) represents how the full-active and semi-active configurations tend to operate more in the maximum efficiency point. Meanwhile, the current of the passive configuration is distributed over the whole range. Fig. 8(b) illustrates the SOC_{SC} evolution along with the driving profile. In the passive configuration, the SOC is more stable due to self-management which determines the FC current as opposed to other configurations that operate in a wider range.
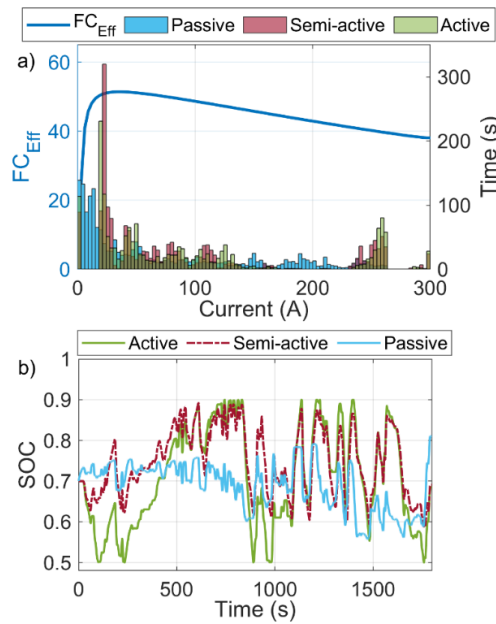

Fig. 8. WMTC test results; a) Current distribution comparison and FC efficiency curve, and b) SOC evolution of the three FC-SC configurations.

The results of component sizing have a strong dependency on the selected driving cycle. In this respect, the optimal size of each configuration is evaluated with a real driving profile. Real driving patterns differ significantly from standard cycles. These profiles might operate in a specific speed range and may not be suitable for design purposes [91]. The real on-road driving cycle presented in Fig. 9(a) has a maximum speed of 110 km/h and a duration of 49 minutes. During this driving profile, the vehicle operates mostly in the high-speed region. Fig. 9 shows the power split after using the real driving cycle. The FC power for all the configuration tends to operate with the same

trend due to the high level of the requested power. Looking at Fig. 9(c), the FC operates more stably in the semi-active configuration. As mentioned earlier, FC normally works in a more distributed way and avoids unnecessary on-off cycles (SDM-SCM-SM modes) as is seen in the second 1452 of active configuration.
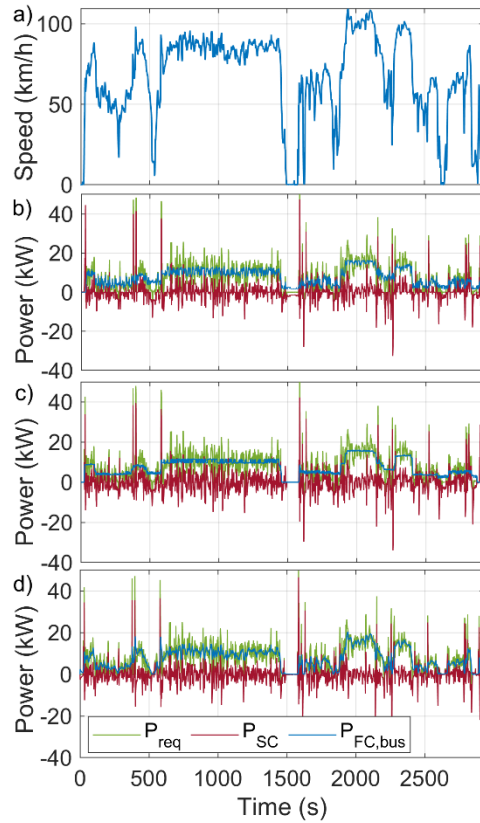

Fig. 9. Power split for the real driving cycle by the optimal size; a) on-road driving cycle b) full-active, c) semi-active, d) passive configuration.

The breakdown of the trip cost obtained from the optimal size for the real driving profile is shown in Table 8. According to this table, the passive configuration has reached the lowest value in terms of trip cost although it has the most expensive FC cost. As previously discussed, the main advantage of the passive configuration resides in the absence of the DC-DC converter.

Table 8. Breakdown of the trip cost for real driving profile

Configuration	H_2 cons.	FC deg.	SC cost	Conv. cost	$Trip$
Full-active	$ 0.81	$ 0.32	$ 0.49	$ 0.41	$ 2.03
Semi-active	$ 0.78	$ 0.48	$ 0.57	$ 0.20	$ 2.03
Passive	$ 0.70	$ 0.62	$ 0.59	-	$ 1.91

The current distribution study presented in Fig. 10(a) shows that the operation of full-active and passive configurations covers most of the FC operating current region while the semi-active configuration has mainly three peaks. The SOC evolution of SC is shown in Fig. 10(b). The full-active configuration can operate in the complete range compared to the other cases because the DC bus voltage value is not related to the SC SOC.
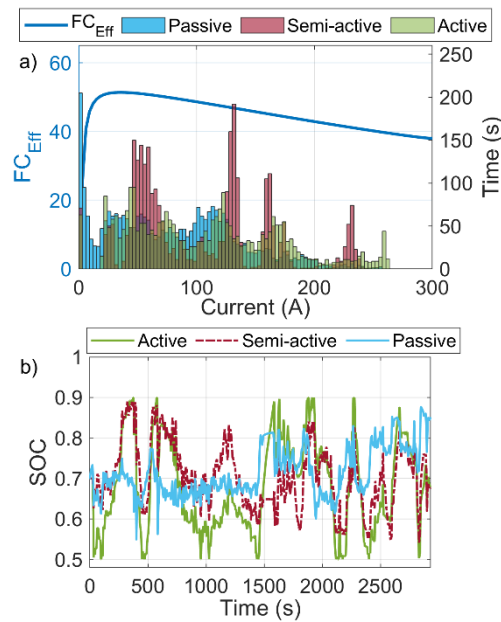

Fig. 10. Real driving cycle test results; a) current distribution comparison and FC efficiency curve, and b) SOC evolution of the three FC-SC configurations.

In order to study the impact of FC degradation, the WMTC profile has been continuously repeated until the FC reaches the EOL. Table 9 summarizes the total travel distance, the total cost of the consumed hydrogen, fuel economy, capital cost of the power supply system, and the equivalent cost per km. It is shown that the full-active configuration has the longest range,

reaching 4% more than semi-active and 10% more than passive configuration. This is due to better management of the FC system that makes it run for a longer time. However, passive configuration has less efficiency losses in the electric conversion that result in an improvement on the fuel economy. Moreover, active configuration is the most expensive in terms of cost per km that is mainly attributed to the high capital cost. The full-active is 20% more expensive than passive, and semi-active is 11% more expensive than passive.

Table 9. Breakdown of the trip cost for the long test profile

Configuration	Eq. range	H_2 cons.	Fuel Econ.	Capital cost	Total cost	Cost per km
Full-active	98088 km	$ 1598	141.1 km/kg	$ 6424	$ 8022	$ 0.082
Semi-active	94315 km	$ 1468	147.7 km/kg	$ 5598	$ 7066	$ 0.075
Passive	88692 km	$ 1220	167.2 km/kg	$ 4721	$ 5941	$ 0.067

5. Conclusions

This paper investigates the performance of three optimized FC-SC configurations, namely: full-active, semi-active, and passive. In this regard, a standard driving cycle is utilized to define the size of the power sources by using a two-step optimization method. A trip cost is defined as the fitness function, which is composed of the FC degradation, consumed hydrogen, and a fraction of the capital cost of the SC and DC-DC converter. Subsequently, the obtained optimal size from the standard driving profile is evaluated based on a real driving profile of the e-TESC 3W electric vehicle. The performed analyses indicate that the trip cost of the proposed passive connection is 14.8% less than the full-active configuration and 6.4% less than the semi-active configuration for the standard driving profile of WMTC. In the case of the real driving cycle, the passive configuration presents 6.3% less cost than the other configurations. It is worth reminding that the passive configuration has a more expensive cost in terms of FC degradation compared to other case studies. However, this cost is compensated by other aspects, such as lower hydrogen consumption and DC-DC converter related prices. In conclusion, based on the presented benchmark study and

simulation test, the passive configuration seems to be the most suitable power source for the Spyder recreational vehicle. As this work has highlighted the potential of the passive topology in a vehicular application, the implementation of this topology on a real test bench should be practiced in future studies.

Acknowledgments

Nomenclatures

Abbreviations

BEV   Battery electric vehicle

DC   Direct current

DoE   US Department of Energy

DP   Dynamic programming

EMR   Energetic macroscopic representation

EMS   Energy management strategy

EOL   End of life

ESS   Energy storage system

FC   Fuel cell

FCEV   Fuel cell electric vehicle

FCHEV   Fuel cell hybrid electric vehicle

GA   Genetic algorithm

HEV   Hybrid electric vehicle

ICE   Internal combustion engine

NWM Normal work mode

OCV Open circuit voltage

PEMFC Proton exchange membrane fuel cell

SC   Supercapacitor

SCM   Supercapacitor mode

SDM   Shutdown mode

SM   Start mode

WMTC World Motorcycle Test Cycle

Variables

$\$DC_{conv}$ DC converter cost

$\$FC_{sys}$ FC system cost

$\$H_2$ Hydrogen cost

$\$SC$ SC cost

$\$Trip$ Trip cost

Δ_{FC} FC degradation percentage

ΔP_{FC} FC slew rate

Δ_{trip} Normalized trip time

Ω_m Rotor rotation speed

A_{aero} Vehicle front area

$C_{O_2}^*$ Oxygen concentration

$C_{SC,u}$ Single SC capacitance

C_{SC} SC equivalent capacitance

C_d Typical aerodynamic drag coefficient

E_{Nernst} Reversible voltage

F_{env} Vehicle traction force resistance

F_{tr} Traction force

G_{gb} Belt transmission drive ratio

H_{FC} Heat transfer coefficient

M_{O_2} Oxygen molar mass

N_{FC} Number of cell FC stacks

$N_{SC,p}$ SC parallel branches

$N_{SC,s}$ SC connected in series

P_{comp} Compressor power

P_{fan} Fan electric power

P_{FC} Fuel cell power

$P_{FC,sys}$ Fuel cell system power

$P_{FC,bus}$ Effective FC power in the DC bus

P_{SC} Supercapacitor power

P_{req} Requested power

Q_{heat} Residual energy

Q_{conv} Heat dissipated due to convection

Q_{max} SC maximum capacity

R_D Equivalent diode resistance

R_{SC} SC equivalent resistor

$R_{internal}$ Internal PEMFC resistor

SOC_{SC} SC level of charge

T_{FC} PEMFC stack temperature

T_{amb} Ambient temperature

$T_{em,r}$ Reference torque

T_{em} Electric machine torque

$V_{EV,max}$ Maximum vehicle speed

W_{H_2} Consumed hydrogen flow

W_{O_2} Oxygen consumed rate

W_{air} Consumed air rate

c_p	Specific heat capacity of air
$i_{FC,max}$	Maximum PEMFC current
i_{SC}	SC current
i_{ts}	Traction system current
k_i	FC degradation coefficient
k_{ti}	Empirical coefficients
m_{eq}	Vehicle mass
p_{H2}	Hydrogen partial pressure
p_{O2}	Oxygen partial pressure
p_{amb}	Ambient pressure
p_{an}	Anode inlet pressure
p_{ca}	Cathode pressure
t_i	Operational time
u_{DC}	DC bus voltage
u_{FC}	PEMFC voltage
u_{SC}	Supercapacitor voltage
u_{act}	Activation loss
u_c	Capacitance element OCV
u_{con}	Concentration loss
u_{ohmic}	Ohmic loss
x_{O_2}	Ideal oxygen mass fraction in the air
ζ_n	Semi-empirical PEMFC resistor parameters
η_{FC}	System efficiency
η_{comp}	Compressor efficiency
η_{gb}	Belt transmission drive efficiency
η_m	motor efficiency
μ_{fr}	Typical rolling resistance coefficient
ξ_n	Semi-empirical activation coefficients
ρ_{air}	Air density

F	Faraday constant
HHV	Hydrogen high heating value
M	DP system work mode
MC_{FC}	Thermal capacity of the FC
r	Wheel radius
x	DP state variable
α	Semi-empirical diffusion mechanism parameter
β	Discrete braking mode value
γ	Specific heat ratio of the air
λ	Oxygen excess ratio constant

References

[1] Y. Wu and L. Zhang, "Can the development of electric vehicles reduce the emission of air pollutants and greenhouse gases in developing countries?," *Transportation Research Part D: Transport and Environment,* vol. 51, pp. 129-145, 2017/03/01/ 2017.

[2] A. Méjean, C. Guivarch, J. Lefèvre, and M. Hamdi-Cherif, "The transition in energy demand sectors to limit global warming to 1.5 °C," *Energy Efficiency,* vol. 12, pp. 441-462, February 01 2019.

[3] S. Campíñez-Romero, A. Colmenar-Santos, C. Pérez-Molina, and F. Mur-Pérez, "A hydrogen refuelling stations infrastructure deployment for cities supported on fuel cell taxi roll-out," *Energy,* vol. 148, pp. 1018-1031, 2018/04/01/ 2018.

[4] Z. Li, A. Khajepour, and J. Song, "A comprehensive review of the key technologies for pure electric vehicles," *Energy,* vol. 182, pp. 824-839, 2019/09/01/ 2019.

[5] A. Sokolov, O. Saritas, and D. Meissner, "Global Market Creation for Fuel Cell Electric Vehicles," in *Emerging Technologies for Economic Development*, D. Meissner, L. Gokhberg, and O. Saritas, Eds., ed Cham: Springer International Publishing, 2019, pp. 131-152.

[6] Y. Wang, B. Seo, B. Wang, N. Zamel, K. Jiao, and X. C. Adroher, "Fundamentals, Materials, and Machine Learning of Polymer Electrolyte Membrane Fuel Cell Technology," *Energy and AI,* p. 100014, 2020/06/29/ 2020.

[7] E. Ruffini and M. Wei, "Future costs of fuel cell electric vehicles in California using a learning rate approach," *Energy,* vol. 150, pp. 329-341, 2018/05/01/ 2018.

[8] G. Wang, F. Huang, Y. Yu, S. Wen, and Z. Tu, "Degradation behavior of a proton exchange membrane fuel cell stack under dynamic cycles between idling and rated condition," *International Journal of Hydrogen Energy,* vol. 43, pp. 4471-4481, 2018/03/01/ 2018.

[9] J. Wang, "System integration, durability and reliability of fuel cells: Challenges and solutions," *Applied Energy,* vol. 189, pp. 460-479, 2017/03/01/ 2017.

[10] M. Bodner, A. Schenk, D. Salaberger, M. Rami, C. Hochenauer, and V. Hacker, "Air Starvation Induced Degradation in Polymer Electrolyte Fuel Cells," *Fuel Cells,* vol. 17, pp. 18-26, 2017.

[11] H. Chen, X. Zhao, T. Zhang, and P. Pei, "The reactant starvation of the proton exchange membrane fuel cells for vehicular applications: A review," *Energy Conversion and Management,* vol. 182, pp. 282-298, 2019/02/15/ 2019.

[12] H. Liu, J. Chen, D. Hissel, J. Lu, M. Hou, and Z. Shao, "Prognostics methods and degradation indexes of proton exchange membrane fuel cells: A review," *Renewable and Sustainable Energy Reviews,* vol. 123, p. 109721, 2020/05/01/ 2020.

[13] M. A. Hannan, M. M. Hoque, A. Mohamed, and A. Ayob, "Review of energy storage systems for electric vehicle applications: Issues and challenges," *Renewable and Sustainable Energy Reviews,* vol. 69, pp. 771-789, 2017.

[14] H. S. Das, C. W. Tan, and A. H. M. Yatim, "Fuel cell hybrid electric vehicles: A review on power conditioning units and topologies," *Renewable and Sustainable Energy Reviews,* vol. 76, pp. 268-291, 2017.

[15] Y. Han, Q. Li, T. Wang, W. Chen, and L. Ma, "Multisource Coordination Energy Management Strategy Based on SOC Consensus for a PEMFC–Battery–Supercapacitor Hybrid Tramway," *IEEE Transactions on Vehicular Technology,* vol. 67, pp. 296-305, 2018.

[16] S. Cheng, L. Xu, K. Wu, C. Fang, J. Hu, J. Li*, et al.*, "Optimal warm-up control strategy of the PEMFC system on a city bus aimed at improving efficiency," *International Journal of Hydrogen Energy,* vol. 42, pp. 11632-11643, 2017/04/20/ 2017.

[17] P. Wu, J. Partridge, and R. Bucknall, "Cost-effective reinforcement learning energy management for plug-in hybrid fuel cell and battery ships," *Applied Energy,* vol. 275, p. 115258, 2020/10/01/ 2020.

[18] H. V. Truong, H. V. Dao, T. C. Do, C. M. Ho, X. D. To, T. D. Dang*, et al.*, "Mapping Fuzzy Energy Management Strategy for PEM Fuel Cell–Battery–Supercapacitor Hybrid Excavator," *Energies,* vol. 13, 2020.

[19] H. Lohse-Busch, K. Stutenberg, M. Duoba, X. Liu, A. Elgowainy, M. Wang*, et al.*, "Automotive fuel cell stack and system efficiency and fuel consumption based on vehicle testing on a chassis dynamometer at minus 18 °C to positive 35 °C temperatures," *International Journal of Hydrogen Energy,* vol. 45, pp. 861-872, 2020/01/01/ 2020.

[20] M. Yue, S. Jemei, R. Gouriveau, and N. Zerhouni, "Review on health-conscious energy management strategies for fuel cell hybrid electric vehicles: Degradation models and strategies," *International Journal of Hydrogen Energy,* vol. 44, pp. 6844-6861, 2019/02/18/ 2019.

[21] Y. Wang, Z. Sun, X. Li, X. Yang, and Z. Chen, "A comparative study of power allocation strategies used in fuel cell and ultracapacitor hybrid systems," *Energy,* vol. 189, p. 116142, 2019/12/15/ 2019.

[22] Y. Liu, J. Liu, Y. Zhang, Y. Wu, Z. Chen, and M. Ye, "Rule learning based energy management strategy of fuel cell hybrid vehicles considering multi-objective optimization," *Energy,* vol. 207, p. 118212, 2020/09/15/ 2020.

[23] M. Kandidayeni, A. O. M. Fernandez, A. Khalatbarisoltani, L. Boulon, S. Kelouwani, and H. Chaoui, "An Online Energy Management Strategy for a Fuel Cell/Battery Vehicle Considering the Driving Pattern and Performance Drift Impacts," *IEEE Transactions on Vehicular Technology,* vol. 68, pp. 11427-11438, 2019.

[24] Y. Zhou, H. Li, A. Ravey, and M.-C. Péra, "An integrated predictive energy management for light-duty range-extended plug-in fuel cell electric vehicle," *Journal of Power Sources,* vol. 451, p. 227780, 2020/03/01/ 2020.

[25] R. E. Silva, F. Harel, S. Jemeï, R. Gouriveau, D. Hissel, L. Boulon*, et al.*, "Proton Exchange Membrane Fuel Cell Operation and Degradation in Short-Circuit," *Fuel Cells,* vol. 14, pp. 894-905, 2014.

[26] D. Arora, C. Bonnet, M. Mukherjee, S. Raël, and F. Lapicque, "Direct hybridization of PEMFC and supercapacitors: Effect of excess hydrogen on a single cell fuel cell durability and its feasibility on fuel cell stack," *Electrochimica Acta,* vol. 310, pp. 213-220, 2019/07/01/ 2019.

[27] K. Gérardin, S. Raël, C. Bonnet, D. Arora, and F. Lapicque, "Direct Coupling of PEM Fuel Cell to Supercapacitors for Higher Durability and Better Energy Management," *Fuel Cells,* vol. 18, pp. 315-325, 2018.

[28] R. C. Samsun, C. Krupp, S. Baltzer, B. Gnörich, R. Peters, and D. Stolten, "A battery-fuel cell hybrid auxiliary power unit for trucks: Analysis of direct and indirect hybrid configurations," *Energy Conversion and Management,* vol. 127, pp. 312-323, 2016.

[29] Q. Xun, Y. Liu, and E. Holmberg, "A Comparative Study of Fuel Cell Electric Vehicles Hybridization with Battery or Supercapacitor," in *2018 International Symposium on Power Electronics, Electrical Drives, Automation and Motion (SPEEDAM)*, 2018, pp. 389-394.

[30] L. Zhang, X. Hu, Z. Wang, F. Sun, and D. G. Dorrell, "A review of supercapacitor modeling, estimation, and applications: A control/management perspective," *Renewable and Sustainable Energy Reviews,* vol. 81, pp. 1868-1878, 2018.

[31] R. Koubaa, S. Bacha, M. Smaoui, and k. Lotfi, "Robust optimization based energy management of a fuel cell/ultra-capacitor hybrid electric vehicle under uncertainty," *Energy,* p. 117530, 2020/04/11/ 2020.

[32] R. Zhang, J. Tao, and H. Zhou, "Fuzzy Optimal Energy Management for Fuel Cell and Supercapacitor Systems Using Neural Network Based Driving Pattern Recognition," *IEEE Transactions on Fuzzy Systems,* vol. 27, pp. 45-57, 2019.

[33] T. Li, L. Huang, and H. Liu, "Energy management and economic analysis for a fuel cell supercapacitor excavator," *Energy,* vol. 172, pp. 840-851, 2019/04/01/ 2019.

[34] Q. Li, B. Su, Y. Pu, Y. Han, T. Wang, L. Yin*, et al.*, "A State Machine Control Based on Equivalent Consumption Minimization for Fuel Cell/ Supercapacitor Hybrid Tramway," *IEEE Transactions on Transportation Electrification,* vol. 5, pp. 552-564, 2019.

[35] Y. Yan, Q. Li, W. Chen, B. Su, J. Liu, and L. Ma, "Optimal Energy Management and Control in Multimode Equivalent Energy Consumption of Fuel Cell/Supercapacitor of Hybrid Electric Tram," *IEEE Transactions on Industrial Electronics,* vol. 66, pp. 6065-6076, 2019.

[36] Z. Sun, Y. Wang, Z. Chen, and X. Li, "Min-max game based energy management strategy for fuel cell/supercapacitor hybrid electric vehicles," *Applied Energy,* vol. 267, p. 115086, 2020/06/01/ 2020.

[37] C. Turpin, D. Van Laethem, B. Morin, O. Rallières, X. Roboam, O. Verdu*, et al.*, "Modelling and analysis of an original direct hybridization of fuel cells and ultracapacitors," *Mathematics and Computers in Simulation,* vol. 131, pp. 76-87, 2017.

[38] S. Ait Hammou Taleb, D. Brown, J. Dillet, P. Guillemet, J. Mainka, O. Crosnier*, et al.*, "Direct Hybridization of Polymer Exchange Membrane Surface Fuel Cell with Small Aqueous Supercapacitors," *Fuel Cells,* vol. 18, pp. 299-305, 2018.

[39] R. Shimoi and Y. Ono, "Fuel cell system," Japan Patent, 2005.

[40] B. Wu, M. A. Parkes, V. Yufit, L. De Benedetti, S. Veismann, C. Wirsching*, et al.*, "Design and testing of a 9.5 kWe proton exchange membrane fuel cell–supercapacitor passive hybrid system," *International Journal of Hydrogen Energy,* vol. 39, pp. 7885-7896, 2014.

[41] B. Phadermrod, R. M. Crowder, and G. B. Wills, "Importance-Performance Analysis based SWOT analysis," *International Journal of Information Management,* vol. 44, pp. 194-203, 2019/02/01/ 2019.

[42] B. L. Cox and C. L. Mutel, "The environmental and cost performance of current and future motorcycles," *Applied Energy,* vol. 212, pp. 1013-1024, 2018/02/15/ 2018.

[43]   A. Macías, M. Kandidayeni, L. Boulon, and J. Trovão, "Passive and Active Coupling Comparison of Fuel Cell and Supercapacitor for a Three-Wheel Electric Vehicle," *Fuel Cells,* 2019/10/29 2019.

[44]   J. P. Trovao, M. R. Dubois, M. Roux, E. Menard, and A. Desrochers, "Battery and SuperCapacitor Hybridization for a Pure Electric Three-Wheel Roadster," in *2015 IEEE Vehicle Power and Propulsion Conference (VPPC)*, 2015, pp. 1-6.

[45]   J. P. F. Trovão, M. Roux, M. É, and M. R. Dubois, "Energy- and Power-Split Management of Dual Energy Storage System for a Three-Wheel Electric Vehicle," *IEEE Transactions on Vehicular Technology,* vol. 66, pp. 5540-5550, 2017.

[46]   A. Bouscayrol, J.-P. Hautier, and B. Lemaire-Semail, "Graphic Formalisms for the Control of Multi-Physical Energetic Systems: COG and EMR," in *Systemic Design Methodologies for Electrical Energy Systems*, I. a. Wiley, Ed., ed, 2012, pp. 89-124.

[47]   M. Kandidayeni, A. Macias, A. A. Amamou, L. Boulon, S. Kelouwani, and H. Chaoui, "Overview and benchmark analysis of fuel cell parameters estimation for energy management purposes," *Journal of Power Sources,* vol. 380, pp. 92-104, 2018.

[48]   M. Kandidayeni, A. Macias, A. A. Amamou, L. Boulon, and S. Kelouwani, "Comparative Analysis of Two Online Identification Algorithms in a Fuel Cell System," *Fuel Cells,* vol. 18, pp. 347-358, 2018.

[49]   A. Kravos, D. Ritzberger, G. Tavčar, C. Hametner, S. Jakubek, and T. Katrašnik, "Thermodynamically consistent reduced dimensionality electrochemical model for proton exchange membrane fuel cell performance modelling and control," *Journal of Power Sources,* vol. 454, p. 227930, 2020/04/01/ 2020.

[50]   B. P. S. Inc., "FCvelocity-9SSL V4.3 Product Manual and Integration Guide," 2017.

[51]   X. Zhao, Y. Li, Z. Liu, Q. Li, and W. Chen, "Thermal management system modeling of a water-cooled proton exchange membrane fuel cell," *International Journal of Hydrogen Energy,* vol. 40, pp. 3048-3056, 2015/02/23/ 2015.

[52]   P. S. Oruganti, Q. Ahmed, and D. Jung, "Effects of Thermal and Auxiliary Dynamics on a Fuel Cell Based Range Extender," *SAE Technical Paper,* 2018.

[53]   I. San Martín, A. Ursúa, and P. Sanchis, "Modelling of PEM Fuel Cell Performance: Steady-State and Dynamic Experimental Validation," *Energies,* vol. 7, 2014.

[54]   J. M. Campbell, *Gas conditioning and processing Volume 2: The Equipment modules*, 9th ed. U.S.A.: PetroSkills, 2014.

[55]   A. Dicks and D. A. J. Rand, *Fuel cell systems explained*: Wiley Online Library, 2018.

[56]   C. Wang, H. He, Y. Zhang, and H. Mu, "A comparative study on the applicability of ultracapacitor models for electric vehicles under different temperatures," *Applied Energy,* vol. 196, pp. 268-278, 2017/06/15/ 2017.

[57]   M. Technologies, "Maxwell Ultracapacitor Cells Product Comparison Matrix," ed, 2020.

[58]   Y. Wang, C. Liu, R. Pan, and Z. Chen, "Modeling and state-of-charge prediction of lithium-ion battery and ultracapacitor hybrids with a co-estimator," *Energy,* vol. 121, pp. 739-750, 2017/02/15/ 2017.

[59]   J. Wang, L. Zhang, J. Mao, J. Zhou, and D. Xu, "Fractional Order Equivalent Circuit Model and SOC Estimation of Supercapacitors for Use in HESS," *IEEE Access,* vol. 7, pp. 52565-52572, 2019.

[60]   H. Lohse-Busch, K. Stutenberg, M. Duoba, and S. Iliev, "Technology Assessment Of A Fuel Cell Vehicle: 2017 Toyota Mirai," Argonne National Lab.(ANL), Argonne, IL (United States)2018.

[61]   C. H. Choi, S. Yu, I.-S. Han, B.-K. Kho, D.-G. Kang, H. Y. Lee*, et al.*, "Development and demonstration of PEM fuel-cell-battery hybrid system for propulsion of tourist boat," *International Journal of Hydrogen Energy,* vol. 41, pp. 3591-3599, 2016/02/09/ 2016.

[62]   H. S. Das, C. W. Tan, A. H. M. Yatim, and S. Li, "Fuel cell and ultracapacitor energy system control using linear quadratic regulator proportional integral controller," *Electrical Engineering,* July 08 2019.

[63]   E. Silvas, T. Hofman, N. Murgovski, L. F. P. Etman, and M. Steinbuch, "Review of Optimization Strategies for System-Level Design in Hybrid Electric Vehicles," *IEEE Transactions on Vehicular Technology,* vol. 66, pp. 57-70, 2017.

[64]   Y. Huang, H. Wang, A. Khajepour, B. Li, J. Ji, K. Zhao*, et al.*, "A review of power management strategies and component sizing methods for hybrid vehicles," *Renewable and Sustainable Energy Reviews,* vol. 96, pp. 132-144, 2018/11/01/ 2018.

[65]   T. Li, H. Liu, H. Wang, and Y. Yao, "Multiobjective Optimal Predictive Energy Management for Fuel Cell/Battery Hybrid Construction Vehicles," *IEEE Access,* vol. 8, pp. 25927-25937, 2020.

[66]   H. Jiang, L. Xu, J. Li, Z. Hu, and M. Ouyang, "Energy management and component sizing for a fuel cell/battery/supercapacitor hybrid powertrain based on two-dimensional optimization algorithms," *Energy,* vol. 177, pp. 386-396, 2019/06/15/ 2019.

[67]   S. Hou, J. Gao, Y. Zhang, M. Chen, J. Shi, and H. Chen, "A comparison study of battery size optimization and an energy management strategy for FCHEVs based on dynamic programming and convex programming," *International Journal of Hydrogen Energy,* 2020/07/01/ 2020.

[68]   M. A. Soumeur, B. Gasbaoui, O. Abdelkhalek, J. Ghouili, T. Toumi, and A. Chakar, "Comparative study of energy management strategies for hybrid proton exchange membrane fuel cell four wheel drive electric vehicle," *Journal of Power Sources,* vol. 462, p. 228167, 2020/06/30/ 2020.

[69]   X. Lü, Y. Wu, J. Lian, Y. Zhang, C. Chen, P. Wang*, et al.*, "Energy management of hybrid electric vehicles: A review of energy optimization of fuel cell hybrid power system based on genetic algorithm," *Energy Conversion and Management,* vol. 205, p. 112474, 2020/02/01/ 2020.

[70]   Y. Zhou, A. Ravey, and M.-C. Péra, "Multi-objective energy management for fuel cell electric vehicles using online-learning enhanced Markov speed predictor," *Energy Conversion and Management,* vol. 213, p. 112821, 2020/06/01/ 2020.

[71]   K. Song, X. Wang, F. Li, M. Sorrentino, and B. Zheng, "Pontryagin's minimum principle-based real-time energy management strategy for fuel cell hybrid electric vehicle considering both fuel economy and power source durability," *Energy,* vol. 205, p. 118064, 2020/08/15/ 2020.

[72]   X. Meng, Q. Li, G. Zhang, T. Wang, W. Chen, and T. Cao, "A Dual-Mode Energy Management Strategy Considering Fuel Cell Degradation for Energy Consumption and Fuel Cell Efficiency Comprehensive Optimization of Hybrid Vehicle," *IEEE Access,* vol. 7, pp. 134475-134487, 2019.

[73]   K. Deb and K. Deb, "Multi-objective Optimization," in *Search Methodologies: Introductory Tutorials in Optimization and Decision Support Techniques*, E. K. Burke and G. Kendall, Eds., ed Boston, MA: Springer US, 2014, pp. 403-449.

[74]   U. S. D. o. Energy, "Fuel Cells," vol. Multi-Year Research, Development, and Demonstration Plan, 2017.

[75]   Z. Song, J. Li, J. Hou, H. Hofmann, M. Ouyang, and J. Du, "The battery-supercapacitor hybrid energy storage system in electric vehicle applications: A case study," *Energy,* vol. 154, pp. 433-441, 2018/07/01/ 2018.

[76]   U. DRIVE, "Electrical and Electronics Technical Team Roadmap," 2017.

[77]   U. S. D. o. Energy, "Hydrogen Production," vol. Multi-Year Research, Development, and Demonstration Plan, 2015.

[78]   S. Galla, A. Szewczyk, J. Smulko, and P. Przygocki, "Methods of Assessing Degradation of Supercapacitors by Using Various Measurement Techniques," *Applied Sciences,* vol. 9, 2019.

[79]   H. Chen, P. Pei, and M. Song, "Lifetime prediction and the economic lifetime of Proton Exchange Membrane fuel cells," *Applied Energy,* vol. 142, pp. 154-163, 2015/03/15/ 2015.

[80]   K. Song, H. Chen, P. Wen, T. Zhang, B. Zhang, and T. Zhang, "A comprehensive evaluation framework to evaluate energy management strategies of fuel cell electric vehicles," *Electrochimica Acta,* vol. 292, pp. 960-973, 2018/12/01/ 2018.

[81]   W. Zhou, L. Yang, Y. Cai, and T. Ying, "Dynamic programming for new energy vehicles based on their work modes Part II: Fuel cell electric vehicles," *Journal of Power Sources,* vol. 407, pp. 92-104, 2018/12/15/ 2018.

[82]   W. Zhou, L. Yang, Y. Cai, and T. Ying, "Dynamic programming for New Energy Vehicles based on their work modes part I: Electric Vehicles and Hybrid Electric Vehicles," *Journal of Power Sources,* vol. 406, pp. 151-166, 2018/12/01/ 2018.

[83]   R. Zhang and J. Tao, "GA-Based Fuzzy Energy Management System for FC/SC-Powered HEV Considering H2Consumption and Load Variation," *IEEE Transactions on Fuzzy Systems,* vol. 26, pp. 1833-1843, 2018.

[84]   T. Li, H. Liu, and D. Ding, "Predictive energy management of fuel cell supercapacitor hybrid construction equipment," *Energy,* vol. 149, pp. 718-729, 2018/04/15/ 2018.

[85]   D. N. Luta and A. K. Raji, "Optimal sizing of hybrid fuel cell-supercapacitor storage system for off-grid renewable applications," *Energy,* vol. 166, pp. 530-540, 2019/01/01/ 2019.

[86]   K. Ettihir, L. Boulon, and K. Agbossou, "Optimization-based energy management strategy for a fuel cell/battery hybrid power system," *Applied Energy,* vol. 163, pp. 142-153, 2016.

[87]   Y. Parvini, A. Vahidi, and S. A. Fayazi, "Heuristic Versus Optimal Charging of Supercapacitors, Lithium-Ion, and Lead-Acid Batteries: An Efficiency Point of View," *IEEE Transactions on Control Systems Technology,* vol. 26, pp. 167-180, 2018.

[88]   R. Álvarez Fernández, S. Corbera Caraballo, F. Beltrán Cilleruelo, and J. A. Lozano, "Fuel optimization strategy for hydrogen fuel cell range extender vehicles applying genetic algorithms," *Renewable and Sustainable Energy Reviews,* vol. 81, pp. 655-668, 2018/01/01/ 2018.

[89]   J. Tao, R. Zhang, and Y. Zhu, *DNA Computing Based Genetic Algorithm: Applications in Industrial Process Modeling and Control*: Springer Nature, 2020.

[90]   E. G. Giakoumis, "Motorcycles," in *Driving and Engine Cycles*, E. G. Giakoumis, Ed., ed Cham: Springer International Publishing, 2017, pp. 167-191.

[91]   J. Brady and M. O'Mahony, "Development of a driving cycle to evaluate the energy economy of electric vehicles in urban areas," *Applied Energy,* vol. 177, pp. 165-178, 2016/09/01/ 2016.